

Laser-driven resonance of dye-doped oil-coated microbubbles: experimental study

Guillaume Lajoinie

*Physics of Fluids Group, MESA⁺ Institute for Nanotechnology,
MIRA Institute for Biomedical Technology and Technical Medicine,
University of Twente, Enschede, The Netherlands*

Jeong-Yu Lee

*Institute of Biomedical Engineering,
University of Oxford, Oxford, United Kingdom*

Joshua Owen

*Institute of Biomedical Engineering,
University of Oxford, Oxford, United Kingdom*

Pieter Kruizinga

*Biomedical Engineering, Thoraxcenter,
Erasmus MC, Rotterdam, The Netherlands*

Nico de Jong

*Biomedical Engineering, Thoraxcenter,
Erasmus MC, Rotterdam, The Netherlands*

Gijs van Soest

*Biomedical Engineering, Thoraxcenter,
Erasmus MC , Rotterdam, The Netherlands*

Eleanor Stride

*Institute of Biomedical Engineering,
University of Oxford, Oxford , United Kingdom*

Michel Versluis

Physics of Fluids Group, MESA⁺ Institute for Nanotechnology,

*MIRA Institute for Biomedical Technology and Technical Medicine,
University of Twente, Enschede, The Netherlands*

(Dated: March 23, 2017)

Abstract

Photoacoustic imaging offers several attractive features as a biomedical imaging modality including excellent spatial resolution and functional information such as tissue oxygenation. A key limitation, however, is the contrast to noise ratio that can be obtained from tissue depths greater than 1-2 mm. Microbubbles coated with an optically absorbing shell have been proposed as a possible contrast agent for photoacoustic imaging, offering greater signal amplification and improved biocompatibility compared to metallic nanoparticles. We have previously developed a theoretical description of the dynamics of a coated microbubble subject to laser irradiation. The aim of this study was to test the predictions of the model. We fabricated two different types oil-coated microbubbles and exposed them to both pulsed and continuous wave (CW) laser irradiation. Their response was characterized using ultra high-speed imaging. Although there was considerable variability across the population, we found good agreement between the experimental results and theoretical predictions in terms of the frequency and amplitude of microbubble oscillation following pulsed excitation. Under CW irradiation, highly nonlinear behavior was observed which may be of considerable interest for developing new photoacoustic imaging techniques with greatly improved contrast enhancement.

PACS numbers: PACS: 80.Qf

I. INTRODUCTION

Over the past decade, photoacoustic (PA) imaging has emerged as a new modality combining the safety and portability of ultrasound imaging with the specificity of optical imaging and offering excellent spatial resolution [1, 2]. PA imaging exploits the photoacoustic effect [3] whereby absorption of modulated electromagnetic radiation leads to heating followed by expansion and contraction of the absorbing material. This results in the generation of a pressure wave and these acoustic emissions can be detected and used to reconstruct an image. The utility of PA imaging has been demonstrated in applications ranging from blood oxygenation mapping to functional brain imaging [4, 5] and is rapidly being translated into pre-clinical use.

The imaging depth, and consequently also the contrast, in PA imaging are quite severely limited by the attenuation of both the optical and acoustic signals in tissue. To address this challenge and also to improve specificity for molecular imaging applications, a number of PA contrast agents have been developed [6–8]. These include dyes such as methylene blue or indocyanine green which give enhanced absorption at specific wavelengths; and also metallic nanoparticles. The latter are of particular interest, as tuning the plasmon resonance characteristics to a particular optical wavelength can lead to effective absorption cross-sections several orders of magnitude larger than those typically obtained from a dye [9]. Concerns about the potential toxicity of nanoparticles have, however hindered their development for clinical use.

A possible alternative for contrast enhancement is to use microbubbles having a gas core of 1-2 μm in diameter, that can be transient or stabilized by a surfactant or polymer coating. These are well established as contrast agents for ultrasound imaging on account of their excellent acoustic scattering cross-section and nonlinear behavior [10, 11]. Phase change microdroplets that turn into bubbles upon laser irradiation have been shown to produce a ten-fold increase in the amplitude of acoustic emissions compared to those produced by nanoparticles [12, 13]. One disadvantage, however, is the large amount of energy required to vaporize the liquid. As photoacoustic imaging advances towards molecular diagnostic [14] and therapeutic imaging applications [15, 16] there is a need for more sensitive and multifunctional contrast agents. Such particles should have a specific PA signature and ideally be visible under other modalities such as ultrasound. Recent work has included the devel-

opment of several photoacoustic microbubbles, i.e stabilized microbubbles coated with an absorbing material that respond to laser excitation [17–25]. Contrast agents have also recently been used in combination with a modulated CW laser that offers extended possibilities in frequency domain photoacoustics [26–30]. Here we propose a photoacoustic microbubble agent, following an analogous principle, that is responsive to both pulsed and CW photoacoustic imaging. We show that, by coating microbubbles with a thin layer of an appropriately selected optically absorbing liquid, the heat deposited during optical irradiation can initiate oscillation of the microbubbles. This can then lead to high amplitude acoustic emissions and requires less energy than the vaporization of liquid droplets. Microbubbles were fabricated in order to exhibit this behavior. Their response was characterized using a combination of ultra high-speed video microscopy and monitoring of acoustic emissions in order to validate the theoretical modeling. The results not only show that such excitation is indeed feasible in practice, but also that close parallels can be drawn between laser-driven and US-driven bubbles.

II. THEORY

The parameters appearing in the equations can be found in Table I.

The details of the theoretical derivation are given in Appendix A. Here, we give the most important results, e.g. the eigenfrequencies and the scaling behavior.

A. Linear theory for the microbubble oscillations

Everywhere, the subscripts w and o refer to the water and the oil, respectively. The microbubble oscillations may be shown to obey a Rayleigh-Plesset type equation of the form:

$$P_g - P_\infty = \ddot{R}_i \left[\frac{R_i^2}{R_e} (\rho_w - \rho_o) + \rho_o R_i \right] + \dot{R}_i^2 R_i \left[\rho_o \left(\frac{3}{2R_i} - \frac{2}{R_e} + \frac{1}{2} \frac{R_i^3}{R_e^4} \right) + \frac{\rho_w}{R_e} \left(2 - \frac{1}{2} \frac{R_i^3}{R_e^3} \right) \right] + 4\mu_o \left[\frac{\dot{R}_i}{R_i} - \frac{\dot{R}_i R_i^2}{R_e^3} \right] + 4 \frac{\dot{R}_i R_i^2}{R_e^3} \mu_w + \frac{2\sigma_{ow}}{R_e} + \frac{2\sigma_o}{R_i}, \quad (1)$$

TABLE I. Physical parameters [31–35] used in the equations describing the response of the bubbles produced in this study. Subscripts 0 or eq designate the initial and equilibrium values, respectively.

symbol	description	DCM value	toluene value	units
$C_{p,o}$	oil heat capacity	1190	1685	J/K/kg
λ_o	oil thermal conductivity	0.14	0.14	W/m/K
ρ_o	oil density	1327	867	kg/m ³
D_o	oil diffusivity	8.9×10^{-8}	1.0×10^{-8}	m ² /s
μ_o	oil viscosity	0.43	0.59	mPa.s
$\sigma_{o,w}$	oil/water interfacial tension	28.3	37.1	mN/m
σ_o	oil surface tension	26.5	28.4	mN/m
symbol	description	value		units
$C_{p,w}$	water heat capacity	4184		J/K/kg
λ_w	water thermal conductivity	0.61		W/m/K
ρ_w	water density	1000		kg/m ³
D_w	water thermal diffusivity	1.5×10^{-7}		m ² /s
μ_w	water viscosity	-		Pa.s
R_i	inner radius	-		m
R_e	outer radius	-		m
x	$\frac{R_i}{R_e}$	-		-
y	$\frac{R_{i,eq}}{R_{i,0}}$	-		-
$V_{w0.1}$	heated water volume	-		m ³
V_{oil}	oil volume	-		m ³
$B_{a,av}$	average power deposited	-		W/m ³
B_a	power deposited	-		W/m ³
P_∞	atm. pressure	100 000		Pa
P_g	gas pressure	-		Pa
T_g	gas temperature	-		K
T_0	room temperature	293		K

where P_g is determined by the heat transfer into and out of the system, and assumes the following expression for the pulsed laser case:

$$P_g = \frac{P_0 R_{i,0}^3}{T_0 R_i^3} T_g = \frac{P_0 R_{i,0}^3}{T_0 R_i^3} \left(T_0 + \frac{F_a}{\rho_o c p_o} H(t) \right), \quad (2)$$

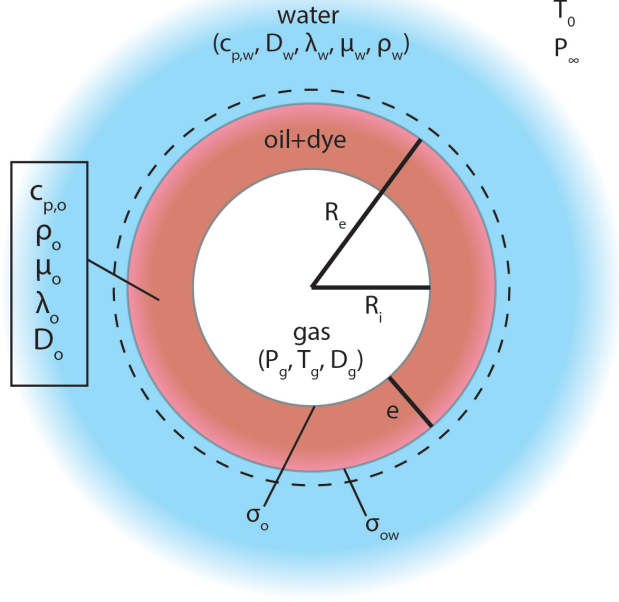


FIG. 1. (color online) Schematic of the microbubble system with the three domains and the corresponding physical parameters.

where F_a is the thermal energy per unit volume deposited by the laser pulse (in J/m^3). The more complex interactions relevant for the CW laser irradiation case are described by:

$$P_g = \frac{P_0 R_{i,0}^3}{T_0 R_i^3} \left[\frac{\int_0^t B_a(t) dt V_{oil}}{\rho_o V_{oil} c p_o + \rho_w V_{w0.1} c p_w} + \frac{B_{a,av}}{3\lambda_o} \left(-1.5 R_{i,eq}^2 + \frac{R_{i,eq}^3}{R_{e,eq}} \left(1 - \frac{\lambda_o}{\lambda_w} \right) + R_{e,eq}^2 \left(0.5 + \frac{\lambda_o}{\lambda_w} \right) \right) + T_0 \right], \quad (3)$$

where $B_a(t)$ is the heat density deposited by the laser (W/m^3). Inserting Eq. 3 into Eq. 1 results in:

$$\alpha B_a - \zeta \dot{R}_i = \ddot{R}_i \beta + 2\gamma \ddot{R}_i \dot{R}_i + \delta \ddot{R}_i + 2\dot{R}_i \epsilon \quad (4)$$

The expression of the coefficients follows directly from Eq. 1 and Eq. 3. Their detailed expression is given in Appendix A18 and A19. The key features of the microbubble behavior can be further described by linearizing Eq. 4 for small bubble oscillation amplitudes and by Fourier transformation to the frequency domain:

$$\frac{r_i}{B_a} = \frac{\alpha/(2\epsilon + \zeta)}{j\omega \left[1 + j\omega \frac{\delta}{2\epsilon + \zeta} - \omega^2 \frac{\beta}{2\epsilon + \zeta} \right]} \quad (5)$$

Here ω is the angular frequency of the laser excitation. The third-order transfer function (Eq. 5) reduces to the product of a resonator transfer function (of order 2) and an integrator $\frac{1}{j\omega}$. In the more simple case of pulsed illumination, the integrator disappears since the driving consists in an quasi instantaneous energy deposition rather than a time modulated power deposition. The gain of the transfer function of Eq. 5 is expressed as:

$$\frac{\alpha_{cw}}{(2\epsilon + \zeta)} = \frac{P_0 R_0^3}{T_0 R_i^3 \left(\rho_o C_{po} + \rho_w \frac{V_{w0.1}}{V_{oil}} C_{pw} \right) \left(2 \left(\frac{-\sigma_{ow}}{R_e^2} + \frac{-\sigma_o}{R_i^2} \right) + 3 \frac{P_g}{R_i} \right)}, \quad (6)$$

and, similarly,

$$\frac{\alpha_{pulsed}}{(2\epsilon + \zeta)} = \frac{P_0 R_0^3}{T_0 R_i^3 \rho_o C_{po} \left(2 \left(\frac{-\sigma_{ow}}{R_e^2} + \frac{-\sigma_o}{R_i^2} \right) + 3 \frac{P_g}{R_i} \right)}, \quad (7)$$

for the case of pulsed irradiation. Here, R_i is the internal bubble radius and V_{oil} is the volume of the optically absorbing liquid surrounding the microbubble. The only other requirement on the encapsulating liquid is that it is immiscible in water. This liquid is hereafter referred to as 'oil'. R_0 is the initial bubble gas core radius. Equations 6 and 7 show that the overall gain of the transfer function is highest for low density and low heat capacity oils. The major determinant of the oscillation amplitude at resonance, however, is the damping coefficient (directly obtained from the canonical transfer function Eq. 5) that was found to depend dramatically on the viscosity of the oil chosen:

$$z \approx \frac{\mu_o + x^3 (\mu_w - \mu_o)}{\sqrt{P_{g,eq} (\rho_o + x (\rho_w - \rho_o))}} \frac{2}{\sqrt{3} R_i}. \quad (8)$$

where $x = R_i/R_e$ is the ratio of the inner to outer bubble radii. Thus the damping coefficient decreases with increasing bubble size, with decreasing layer thickness (in competition with the laser energy absorption), and, primarily, with decreasing oil viscosity. This relation emphasizes the necessity for using low viscosity oils.

B. Undamped natural frequency

The undamped natural frequency of the system follows directly from the expression of the linear resonance curve (Eq. 5) as follows:

$$f_0 = \frac{1}{2\pi R_i} \sqrt{\frac{\frac{2}{R_i} (2\sigma_o + \sigma_{ow} (3x - x^2)) + 3P_\infty}{x(\rho_w - \rho_o) + \rho_o}}, \quad (9)$$

A crucial feature of this expression is the dominance of R_i , the instantaneous or 'hot' bubble radius, in determining the natural frequency. Also, the influence of the oil density, which is present in the denominator, can shift significantly the natural frequency, whereas the surface tension only has a secondary effect.

C. Scaling function

One challenge in comparing the results from the theoretical model to the experimental data is the difficulty in fully characterizing the system. For example, the variations in thickness of the oil layer within individual microbubbles is extremely difficult to measure. Some influences, however, such as differences in the absorption of individual microbubbles (i.e. encapsulation efficiency) and potential inhomogeneities in the irradiating laser beam due to its finite size can be compensated for by expressing the amplitude at resonance:

$$\underline{r_i} = \frac{-B_a \alpha \beta}{(2\epsilon + \zeta) \delta}, \quad (10)$$

and looking at its dependency on thermal dilatation, which can be measured experimentally and individually for each bubble. This results in a scaling function that compensates for the influence of variations in most of the parameters:

$$\underline{r_i} \propto y - \frac{1}{y^2}, \quad (11)$$

where the variable $y = \frac{R_{i,eq}}{R_{i,0}}$ is a measure of the thermal dilatation of the microbubble that can be obtained from the optical recordings. This scaling function therefore enables comparison between the recorded individual bubble responses and their predicted behavior.

The remaining influences in the bubbles responses such as the influence of an unknown oil layer thickness that varies from bubble to bubble will not allow for a prediction of a single line but of an area wherein the individual bubble responses are expected to fall. This area does not depend on their absorbance nor on the conditions of irradiation. Higher control over the microbubble fabrication process and properties will therefore directly result in narrowing this area and further refine the understanding of the experimental results.

III. MATERIALS AND METHODS

A. Materials

Albumin from bovine serum (BSA), Oil red, Nile Red, dichloromethane (DCM) and toluene were purchased from Sigma-Aldrich (Bornem, Belgium). Perfluoropentane (PFP, 99%) was obtained from Fluoromed (Round Rock, TX, USA). All chemicals were of reagent grade and used without further purification.

B. Microbubble preparation

In this pilot study, we coated the microbubbles with a selection of two oils, dichloromethane and toluene, that can be readily incorporated into the microbubbles. The properties of the oils are given in Table I. To prepare a saturated dye solution, 50 mg of oil red was dissolved in 1 mL of DCM. The solution was stirred for 10 min and excess oil red removed by allowing sufficient time for separation from the DCM. Then, 10 μ L of PFP was mixed with 200 μ L of the oil red solution. The mixture was added to an aqueous solution of BSA (1 mg/mL) and sonicated using a probe sonicator (Bandelin Sonorex HD3200) with the tip held in the center of the vessel for 5 sec and at the air/liquid interface for 15 sec. The prepared bubbles were extracted using a syringe and dispersed in 20 mL of deionized water. To make BSA/toluene bubbles, the same volume of toluene was used instead of DCM, and the process was repeated. The microbubbles were not centrifuged as for these experiments the microbubble radius was a study parameter and so it was desirable to have wide size distribution from which individual microbubbles of particular sizes could be selected.

C. Scaling

The scaling function given in the previous section was applied to the theoretical prediction after correction by a factor $1/1.7$ to account for the non fully-stable thermal state of the microbubble after $200\ \mu\text{s}$. This number originates from considering heat transfers at a finite time in the experiments, whereas a fully stable regime is assumed in the theory.

D. Confocal microscopy

In order to estimate the thickness of the oil layer that encapsulates the microbubbles, a fluorescently labeled batch was produced. Nile Red dye was chosen for this purpose. Confocal microscopy images were taken of ~ 100 microbubbles for each formulation. The thickness of the oil layer was extracted by measuring the $1/e$ width of the Gaussian fit of the fluorescence intensity surrounding the microbubbles (Fig. 2b) using a script written in Matlab. The thickness of the oil layer for the toluene-coated microbubbles was estimated at $1.77\ \mu\text{m}$ with a standard deviation of $0.37\ \mu\text{m}$ and that of the DCM-coated microbubbles was estimated at $1.92\ \mu\text{m}$ with a standard deviation of $0.32\ \mu\text{m}$. The bubble radius ranged from $\sim 1\ \mu\text{m}$ to $\sim 20\ \mu\text{m}$ and no obvious dependency of the oil layer thickness in the bubble size was found.

E. Experimental setup

The combined optical and acoustical behavior of the microbubbles was studied by introducing a diluted suspension into an OpticellTM cell culture device, consisting of two optically and acoustically transparent membranes in a rigid frame. The Opticell was immersed in a water bath at room temperature and laser illumination was provided using a frequency-doubled Nd:YAG pulsed laser (Evergreen, 150 mJ) that was used for pulsed excitation (pulse width $\Delta t = 8\ \text{ns}$, $\lambda = 532\ \text{nm}$) and a CW diode-pumped solid-state laser (2 Watt, $\lambda = 532\ \text{nm}$, Changchun New Industries) that was used for CW excitation. The laser was focused onto a $40\ \mu\text{m}$ diameter spot within the Opticell through a water-immersion objective (LUMPLFL, $60\times$, NA=0.9, Olympus). The Brandaris 128 ultra high-speed camera [36, 37] was used to take optical recordings (128 images) of individual microbubbles through the same objective at frame rates of ~ 10 million frames per second. Illumination was provided by a Xenon

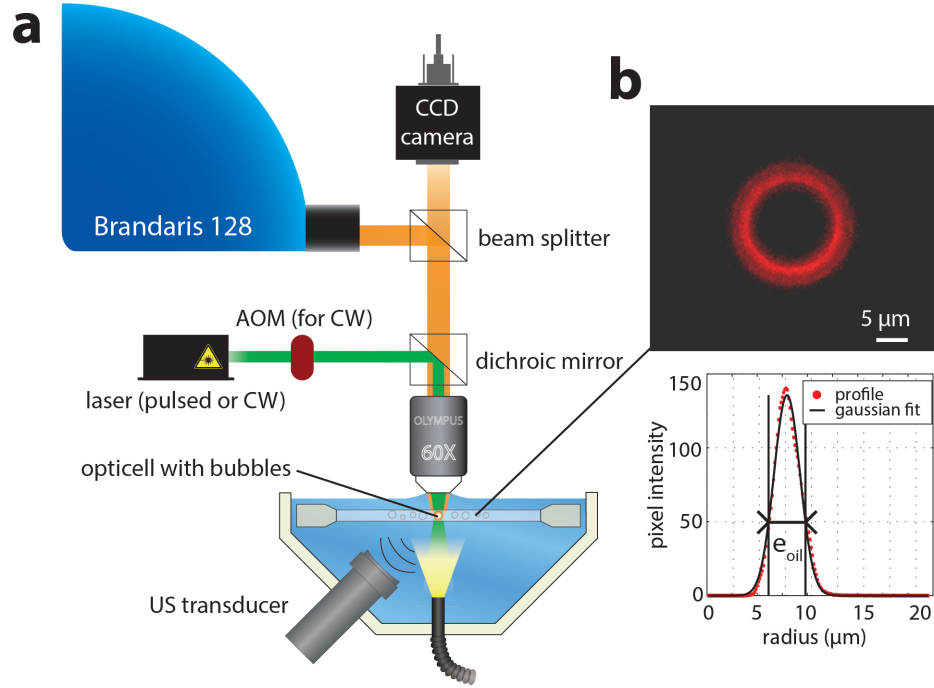


FIG. 2. (color online) **a** Schematics of the experimental setup comprising the ultra high-speed camera Brandaris 128, a pulsed or CW laser coupled through a microscope objective, and a 1 MHz ultrasound receiving transducer to record the acoustic emission from the microbubbles. **b** Example of confocal image of an oil-coated microbubble where the oil is labeled with fluorescent Nile Red.

flash light (EG&G, FX-1163, Perkin Elmer Optoelectronics, Salem, MA).

For the pulsed laser irradiation experiments, the laser was first fired only in the second of the series of 6 movies (sequence of 128 images) recorded by the Brandaris camera, so that the first movie would provide a reference. The pulsed laser was fired for a total of three times at low energy setting ($\sim 50 \text{ mJ/cm}^2$). The laser output before entering the microscope was set close to the minimum ($\sim 3 \text{ mJ}$, calibrated using a Coherent FieldMax_{II} laser energy meter) and further reduced using neutral density filters (ND 1.65).

The CW laser output was modulated in time at a chosen frequency by an acousto-optic modulator (AA-optoelectronics, France). The CW laser was turned on $233 \mu\text{s}$ before the start of the high-speed recording and the AOM was triggered to transmit the laser light onto the sample $200 \mu\text{s}$ before the start of the Brandaris recording to allow for the bubbles to reach a quasi-stable thermal state. Each bubble was irradiated 5 times consecutively with a 100 ms time interval. Toluene-coated and DCM-coated microbubbles were irradiated with a 0.75 MHz modulated laser beam in order to study the effect of variations in the physical properties of the coating. The DCM-coated bubbles were irradiated by a 1.0 MHz

and 0.75 MHz modulated laser in order to investigate the effect of the frequency change.

The acoustic signals emitted by the vibrating microbubbles were collected by a 1 MHz (90% bandwidth) focused broadband transducer (C302, Panametrics) located at the bottom of the water tank, then fed into a pre-amplifier and stored using a digital oscilloscope (DPO3034, Tektronix). The optical focus and the acoustic focus were co-aligned using a 0.2 mm diameter needle hydrophone (Precision Acoustics, UK). Here, we study bubbles with radii between 2 and 6 μm , which is a relevant size for imaging contrast agents. Such bubbles are also easily imaged under a microscope. The expected resonance frequency for this size range is close to 1 MHz, and this determined our choice of transducer center frequency. Using the bubble size as a study parameter further required the use of a broadband transducer. In the CW laser experiment, the large bandwidth of the transducer allowed for the simultaneous extraction of the harmonic and subharmonic signals. We chose a focused transducer for its advantage in sensitivity.

F. Data processing

1. Pulsed laser irradiation

The radius-time curves describing the response of the microbubbles to the pulsed laser irradiation were extracted from the ultra-high speed movies using a custom written Matlab script (version R2012a, The MathWorks, Natick, MA) implementing a combination of contrast correction, thresholding and area detection. This analysis method showed good stability despite the variations in illumination intensity across the recording. A second script was used to extract the properties defining the microbubbles oscillatory behavior, through fitting of the experimental data to the following equation describing the impulse response of a damped oscillator [38, 39]:

$$R(t) = R_0 + Ae^{-z\omega_0(1-z^2)t}\sin(\omega_0\sqrt{1-z^2}t). \quad (12)$$

Here A is the amplitude of the response, z is the damping coefficient of the oscillator and ω_0 its eigenfrequency. t is the time, R_0 is the initial bubble radius. The script implements an error minimization based on a discrete variation of the parameters A , z and ω_0 . Discrete steps of 10^{-2} for the damping coefficient, 10 nm for the amplitude and 10 kHz for the

frequency were chosen. This approach allows for a more robust analysis while ensuring the required precision.

2. CW laser irradiation data

The radius-time curves of the bubble responses from the high-speed recordings were extracted using the same Matlab script as for the pulsed excitation. The frequency content and corresponding amplitude of the oscillations were then extracted using fast Fourier transform analysis (fft). The phase of the oscillations was determined by fitting a sine wave to the microbubble oscillations. Both operations were performed in Matlab.

The pressure emission curves recorded by the 1 MHz transducer and corresponding to the first CW laser irradiation were all analyzed using the fast Fourier transform function in Matlab also for the harmonics and subharmonics. The transducer was calibrated in emission by sending a chirp wave to a needle hydrophone (0.2 mm, Precision Acoustics) placed at the focus of the transducer. Then a perfect reflector (stainless steel) was placed at the focus of the transducer to measure the receive characteristics using the same chirp wave [40]. Finally, the conversion of the time to a bubble radius was performed with the help of a finite differences simulation of the heat transfers using the method described previously [12]. During the CW laser irradiation, the bubble heats up and grows in time following a function $f(1/\tau)$ with $\tau = R_{ieq}^2/D_w$ with τ the typical time scale, D_w the thermal diffusivity of water and R_{ieq} the equilibrium radius of the bubble, which is also equal to the thickness of the thermal boundary layer at equilibrium [12]. The function f is given by the finite differences simulation. The conversion is finally achieved by using the two reference points given by the cold initial radius of the microbubbles measured in the first high-speed recording (laser off) and the average hot radius of the microbubble after 200 μs of heating measured in the second high-speed recording, i.e. at the first laser irradiation.

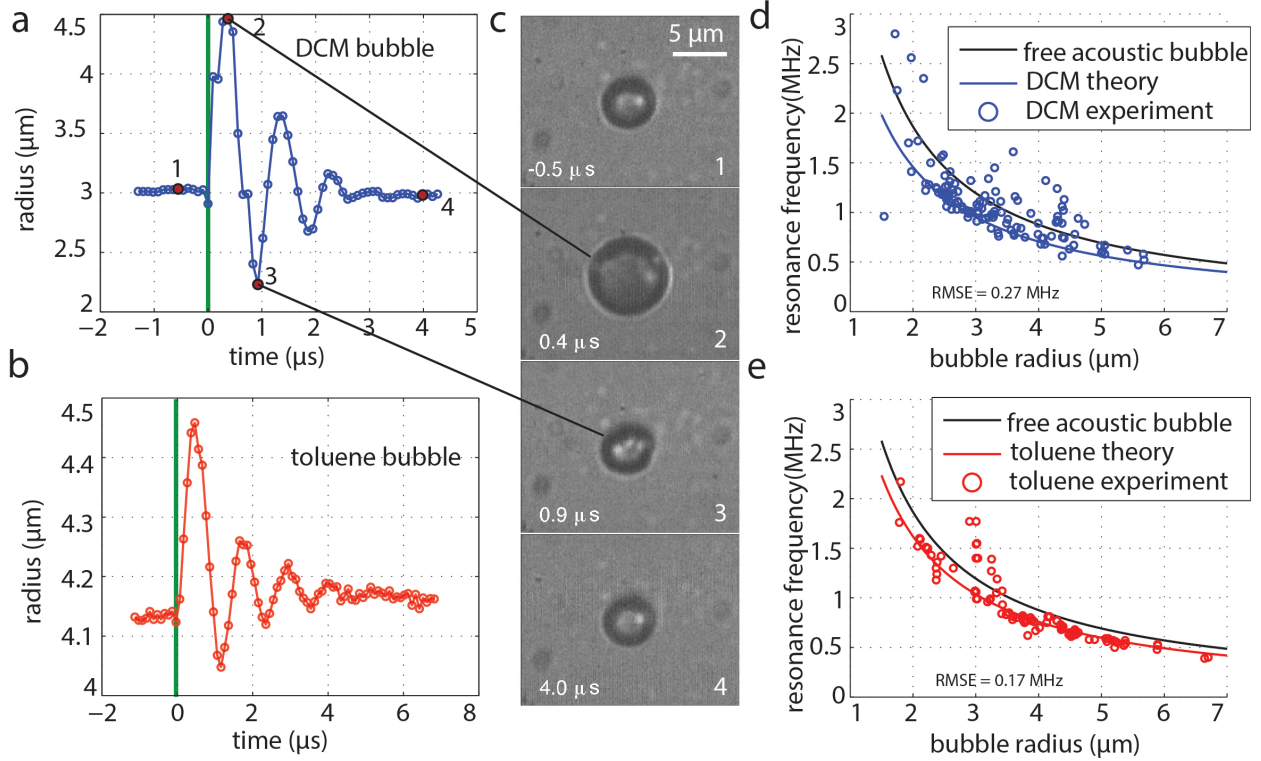


FIG. 3. (color online) **a** and **b** Example of response of a DCM-coated (**a**) and toluene-coated (**b**) microbubbles to $\sim 50 \text{ mJ/cm}^2$ pulse laser irradiation. The arrival of the laser pulse is indicated by the vertical green line. **c** Frames of the ultra-high speed recording of the event plotted in **a**. **d** and **e** Theoretical and experimental resonance frequencies of DCM and toluene-coated microbubbles, respectively. R-P in the legend corresponds to the Rayleigh-Plesset equation for a free, acoustically driven bubble.

IV. RESULTS

A. Pulsed irradiation

1. Experimental bubble response

The aim of the pulsed laser experiments was to examine the impulse response of the microbubbles and to extract their oscillatory behavior. Two examples of impulse responses of DCM and toluene-coated microbubbles are displayed in Figs. 3a [41] and b [42], respectively, derived from the ultra high-speed optical recordings. The laser pulse of 8 ns hits the microbubble at $t = 0$. During the pulse, the oil quickly heats up and transfers the thermal energy to the microbubble gas core, thereby initiating the microbubble oscillations. Example frames from the optical recording of a DCM-coated microbubble are shown in Fig. 3c.

The same experiment was reproduced to obtain 66 individual responses for the toluene-coated microbubbles and 57 for the DCM-coated microbubbles. The corresponding undamped natural frequencies ω_0 for each bubble were extracted by fitting Eq. 12 to the radius-time curve. The results are shown in Figs. 3d and e with a root mean square error of 0.27 MHz and 0.17 MHz, respectively. The theoretical undamped natural frequencies were calculated from Eq. 9 and are also plotted in Figs. 3d and e.

The choice of the simple impulse response equation (Eq. 12) is justified, since the timescales of heat deposition, cooling and oscillations are decorrelated. In practice, this decorrelation implies that the core temperature is oscillating around a 'hot' temperature instantly produced by the laser impulse. As a response to this impulse excitation, the bubble oscillates while cooling down on a much slower timescale. The theoretically computed microbubble undamped natural frequencies agree very well with the measured values for both microbubble populations. The difference between the undamped natural frequencies of both microbubble populations can also clearly be seen in Figs. 3d and e.

The toluene-coated microbubbles exhibited a damping coefficient of $z = 0.148^{+0.15}_{-0.1}$ whilst for the DCM-coated microbubbles it was significantly higher $z = 0.247^{+0.15}_{-0.15}$, which is expectedly much higher than the theoretical value for a bubble free of BSA. Such result is also well known for acoustically driven bubbles. For the measured range of bubble sizes and oil thicknesses, the oil-coated bubble free of BSA has a damping coefficient from Eq. 12 $z = 0.0175^{\pm 0.0055}$ for the toluene-coated microbubbles and $z = 0.0119^{\pm 0.0036}$ for the DCM-coated microbubbles. It is also likely that partial phase change of these relatively volatile oils impacts on the damping coefficient.

B. CW laser irradiation

1. Experimental bubble response

An example of optically recorded response of a DCM-coated microbubble to CW laser irradiation is shown in Figs. 4a-c. The first recording was taken before the laser was on thereby displaying the size of the 'cold' bubble.

As indicated in Fig. 4a [43] and in selected frames, Figs. 4b and c, the average size of the microbubble when exposed to the laser light increases significantly. Clear oscillations around

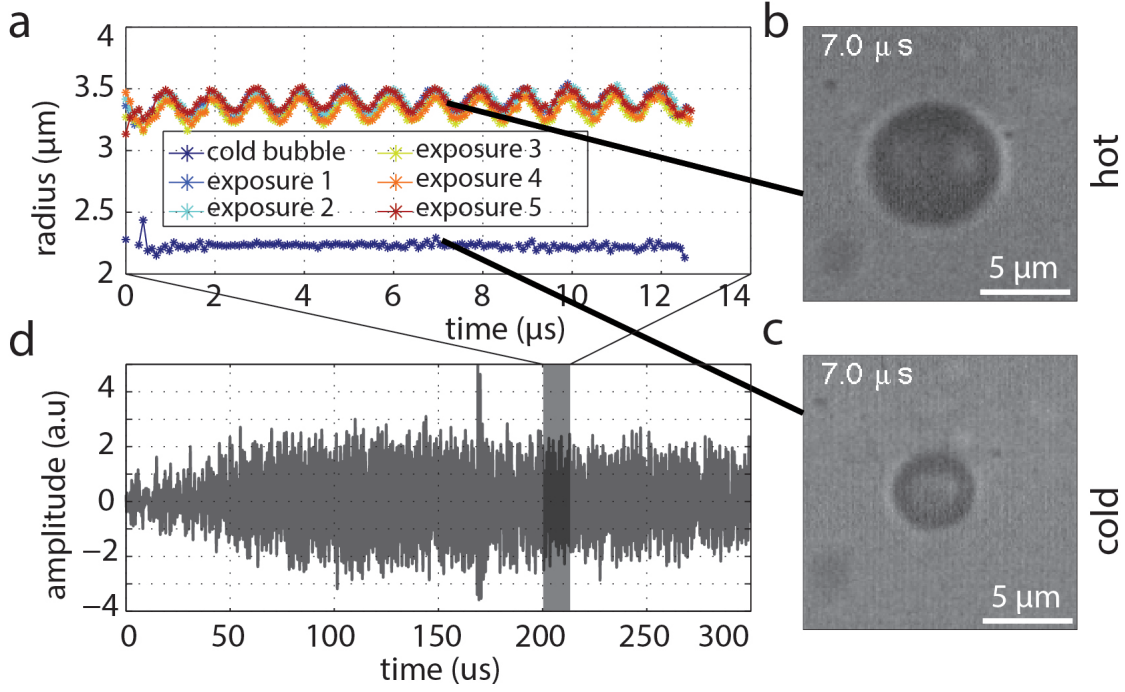


FIG. 4. (color online) **a** Radius-time curve of a DCM-coated microbubble extracted from an ultra high-speed optical recording. **b** and **c** Still frames of the optical recording used to obtain **a**. **b** is taken from the first movie, before the laser is turned on and shows the 'cold' bubble. **c** is taken from the first laser irradiation and when the radius of the bubble coincides with the average radius. **d** displays the acoustic emission from a DCM-coated microbubble over the full 300 μs of laser irradiation recorded by the 1 MHz focused ultrasound transducer. The position in time and duration of the high-speed recording is depicted by the grey rectangle.

this average radius are also visible in Fig. 4a. These oscillations are a direct consequence of the modulation of the laser intensity. The bubble was further irradiated for 100 μs , i.e. for a total of 300 μs , during which the vibrating microbubble emits an ultrasound wave that was recorded by the receiving transducer positioned at the bottom of the water tank. An example of the acoustic emission from a DCM-coated microbubble irradiated by a 1 MHz modulated laser is displayed in Fig. 4d. The acoustic trace has been filtered in the Fourier domain to remove the high frequency noise arising from the electronics.

2. Single microbubble resonance

Fig. 4b and c show the increase in the microbubble size between 2 time points. In fact, the microbubbles are growing continuously during the 300 μs during which the laser is on. Thus, in some cases, the microbubble will grow from below the resonant size to above the

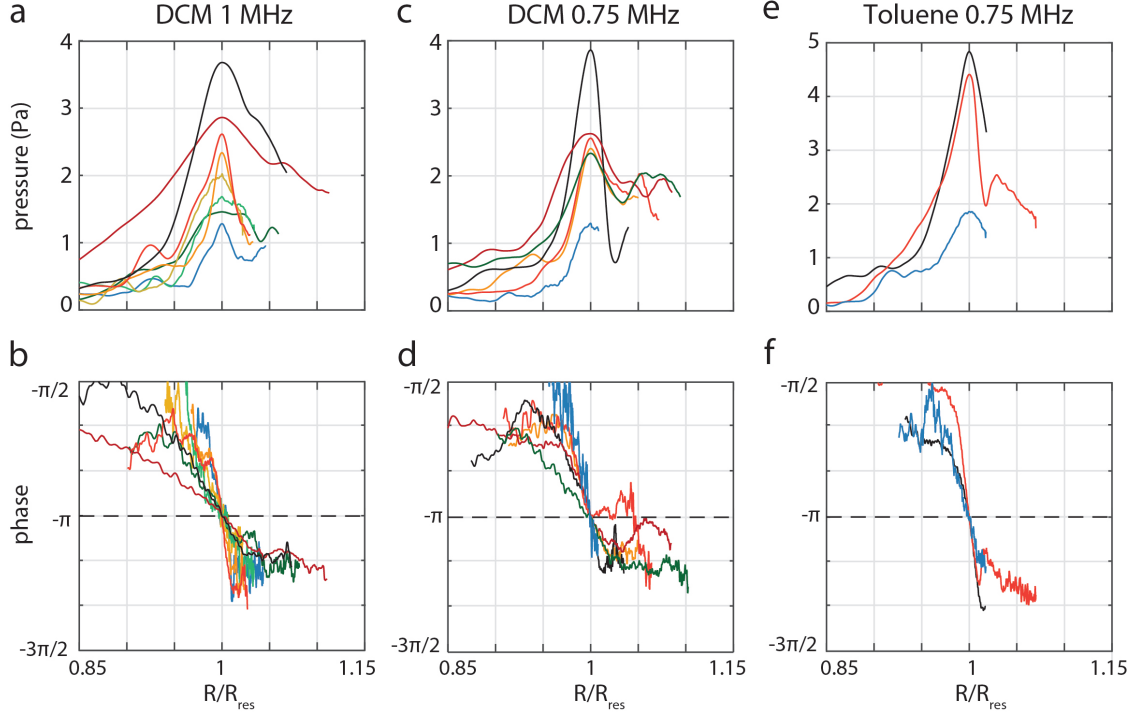


FIG. 5. (color online) **a**, **c** and **e** Sample of resonance curves of single microbubbles obtained from a single acoustical recording when a microbubble, heated up by the average irradiating laser power, grows from below the resonant size to above the resonant size. Each color represent a different bubble. **a**, **c** and **e** correspond to DCM-coated microbubbles irradiated by a 1 MHz and 0.75 MHz modulated CW laser and toluene-coated microbubbles irradiated by a 0.75 MHz modulated CW laser, respectively. **b**, **d** and **f** show the phases of the oscillations for each curve of **a**, **c** and **e**, respectively.

resonant size thereby describing its own resonance curve. This feature cannot be optically captured as no existing optical system can record the phenomenon with sufficiently high time resolution over such a long duration. The ultrasound transducer, however, can capture these events via the pressure emitted by the microbubble during the entire duration of the laser exposure. Knowing the size of the bubble at two time points from the optical recordings, these acoustic emission curves can be processed in order to retrieve the full resonance curve of a single bubble from a single CW laser exposure. The details are given in the Methods section.

A sample of such resonance curves is given in Fig. 5 for DCM-coated microbubbles irradiated by a CW laser modulated at frequencies of 1 MHz (Fig. 5a and b) and 0.75 MHz [44] (Fig. 5c and d) and toluene-coated microbubbles irradiated by a CW laser modulated at 0.75 MHz (Fig. 5e and f). The horizontal axis give the radius of the bubble normalized

by its resonant radius. It is clearly visible in Fig. 5 that the resonance is correlated with a strong shift in the phase of the received pressure wave, as expected for a resonating system. It is also clear that individual microbubbles can display significantly different behavior from one another and the resonance frequency of each can vary by as much as 15% from the predicted theoretical value. The mean resonant size measured from the resonance curves was $3.42 \pm 0.23 \mu\text{m}$, $4.13 \pm 0.27 \mu\text{m}$ and $4.31 \pm 0.53 \mu\text{m}$ for the DCM bubble excited at 1.0 MHz, the DCM bubbles excited at 0.75 MHz and the toluene bubbles excited at 0.75 MHz, respectively. The theoretical values given in the same order are $2.89 \mu\text{m}$, $3.81 \mu\text{m}$ and $4.03 \mu\text{m}$. Note that this deviation from the theoretical predictions was not observed when the bubble is irradiated with a pulsed laser. Also as observed from the impulse response of the microbubbles, the damping is significantly different for each microbubble as is evident from the various widths of the individual resonance peaks.

3. Microbubble population response

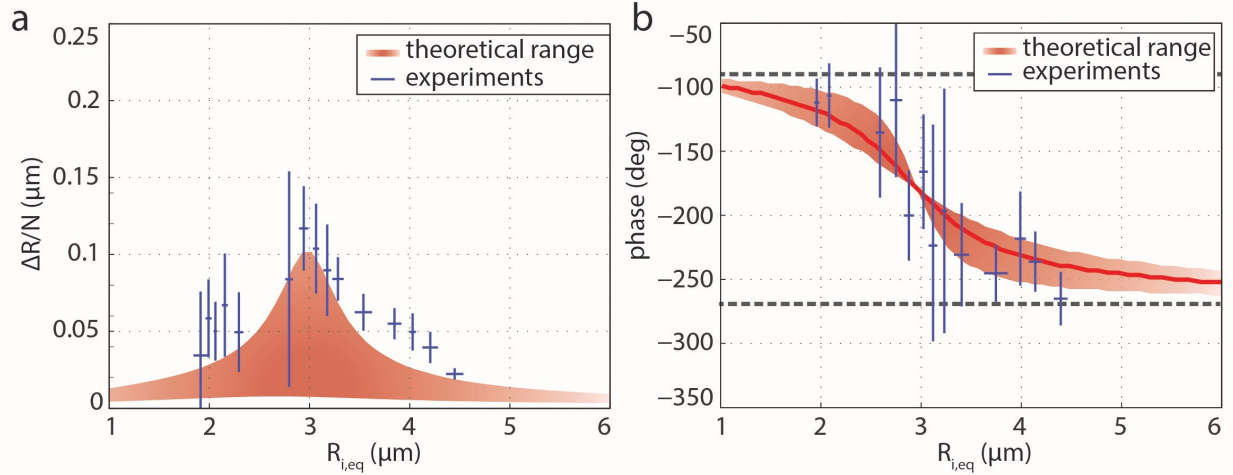


FIG. 6. (color online) **a** Predicted resonance behavior of a population of DCM-coated microbubbles to a 1 MHz modulated CW laser (red area) given the experimentally measured damping coefficients for the considered microbubbles. Experimental data extracted from the ultra high-speed recordings are represented with blue error bars. The data in both cases is normalized using the proposed scaling function. **b** Relative phase of the microbubble oscillations corresponding to the data shown in **a**.

In order to better understand the behavior of the microbubble population as a whole, we now look at the response of each bubble at a single time point given by the optical recording.

By doing so, we look at the global behavior of such laser-driven microbubbles. The influence of the variation in absorbance from one microbubble to another can be compensated for using Eq. 11. Using the range of damping coefficients measured from the impulse response of the microbubbles, a theoretical range for the microbubble responses can be calculated. This range is represented by the red area in Fig. 6a. On the same graph, the response of the microbubbles is represented by blue error bars. They represent the standard deviation per bin of 10 bubbles. Overall, the microbubbles show a stronger response than predicted. This is once more probably due to a partial vaporization/condensation of the oil layer, which absorbs part of the pressure variations in the core of the microbubble and thus allows for a larger oscillation amplitude. Despite this discrepancy, the resonant radius and the relative phase shift shown in Fig. 6b are in reasonable agreement with the expected behavior.

4. Harmonic and subharmonic generation

The resonance phenomenon shown in Fig. 6 is based on the response of the microbubbles at the fundamental frequency, i.e. that of the laser modulation. Just as in the case of acoustic excitation, the microbubbles also generate at harmonic and subharmonic frequencies due to the intrinsic non-linearity of their volumetric oscillations. The non-linearities are known to be further strengthened by the presence of the coating (surfactant, protein or phospholipid for example) necessary to stabilize the microbubbles long enough to use them in practice [45]. Fig. 7 shows the amplitude of the first harmonic and of the subharmonic generated by a microbubble as a function of its size. The same bubbles as those depicted in Fig. 5 are used here and the horizontal axis is scaled to the resonant radii of the individual microbubbles.

From the results it appears that the harmonic generation mostly occurs around resonance (Fig. 7a, c and e) with an amplitude up to -10 dB as compared to the fundamental, which makes them practically usable. Furthermore, only a few bubbles did not generate a significant second harmonic. Interestingly, the generation of subharmonic components was not highest from bubbles of resonant size but in the case of DCM-coated microbubbles for radii $\sim 10\%$ bigger for the DCM-coated microbubbles (Fig. 7b and d). In some cases the subharmonic was actually larger than that at the fundamental frequency, with a maximum of +8 dB. A positive sub-harmonic generation on a dB scale practically implies that the microbubble experiences a period doubling as observed in a few optical recordings. This

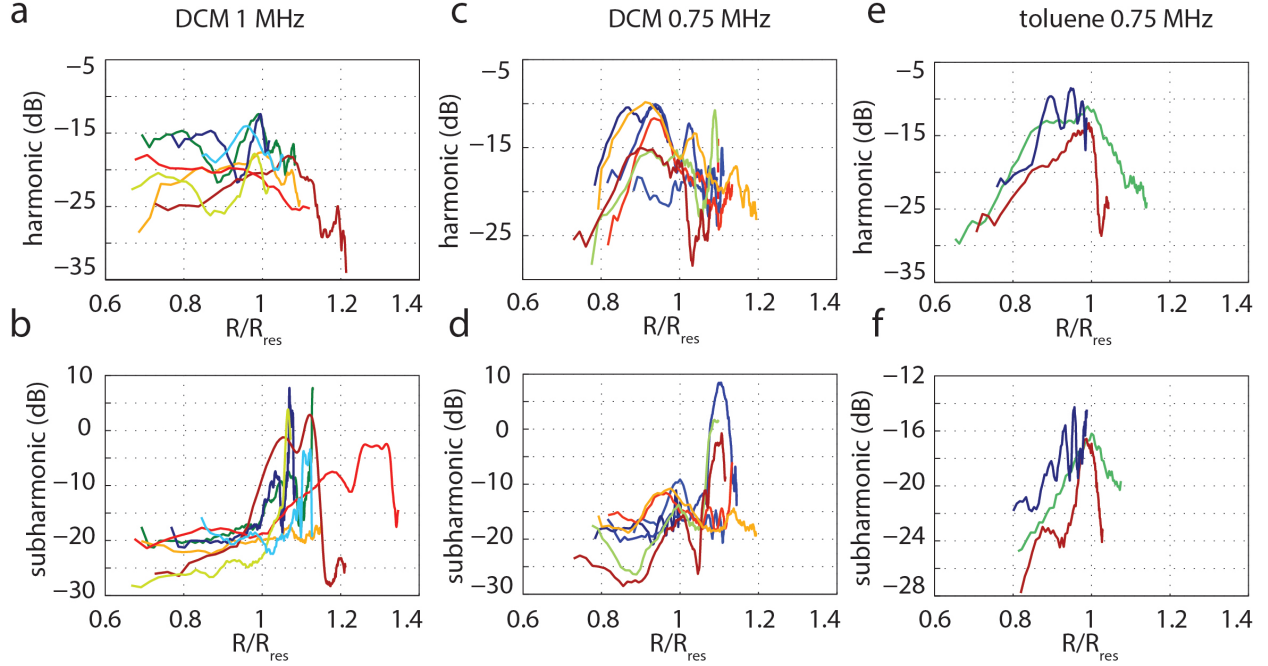


FIG. 7. (color online) **a**, **c** and **e** Harmonic generation obtained from the acoustical recordings when a single microbubble, heated up by the average irradiating laser power, grows from below the resonant size to above the resonant size. **a**, **c** and **e** correspond to DCM-coated microbubbles irradiated by a 1 MHz and 0.75 MHz modulated CW laser and toluene-coated microbubbles irradiated by a 0.75 MHz modulated CW laser, respectively. **b**, **d** and **f** show the sub-harmonic generation in the same order. The x-axis displays the radius of the microbubble normalized by its resonant radius. The emitted pressure is plotted in the vertical (in dB) with the maximum response at the fundamental frequency as a reference.

effect was not observed for the toluene-coated microbubbles (possibly due to the smaller number of bubbles growing across their resonant size) and could be a result of the higher volatility of the DCM as compared to the toluene.

V. DISCUSSION

In the experiments described in this study, the exposure lasts for 200 μ s before the first recording is taken. Also from the finite difference simulation, we know that a resonant bubble at 1 MHz reaches 73% of the final thermal equilibrium radius after 100 μ s and 79% in 200 μ s which represents only a small difference. After a short time ($< 100 \mu$ s) the system temperature rises very slowly (due to the spherical configuration), and the bubble grows to 95% of its final equilibrium size in tens of milliseconds. This problem can be addressed theoretically

more rigorously by setting the equilibrium radius to be time dependent, and considering its variations to be slow compared to the timescale of the oscillations. Strictly speaking, however, this treatment should be combined with a treatment of the partial vaporization of the fluids that is for now the main imprecision of the proposed model. Further development of the theoretical model must include vaporization and molecular diffusion, which are both relevant at longer irradiation timescales. It is important to note here that the differences observed between the theoretical resonant radius and the measured one can partly result from the addition of the imprecisions arising when simulating the bubble heating without Rayleigh-Plesset dynamics. This is expected to have a minor effect on the measurement, as compared to the effect of the partial vaporization of the oil.

With regard to the materials used, the liquids chosen for the purposes of these experiments are referred to as oils. It is to be noted that these are not necessarily oils in the chemical sense, and are only required to be immiscible with water. It is also clear that DCM and toluene are not biocompatible liquids, but they offer the advantage of being well characterized and easy to handle. The positive results obtained in this paper provides strong motivation to develop formulations consisting of more biocompatible oils. These oils should also be less volatile. In terms of safety, the microbubbles were seen to be highly responsive at low laser energy: the energy used for the pulsed excitation was $\sim 50 \text{ mJ/cm}^2$ well within the range considered safe for medical use [46] within the biological window ($\sim 1000 \text{ nm}$). The use of CW lasers offers many advantages in term of costs, ease of use, signal to noise ratio, and allows for making use of some rather unique features as demonstrated above. It also requires, however, higher levels of energy deposition by the laser. We estimate the intensity of the CW laser used for these experiments to be between 50 and 500 kW/cm^2 which, integrated over the irradiation time is too high for safe use. Furthermore, after 200 microsecond of laser irradiated, less than ten percent of the input energy is stored in the bubble itself, which limits the efficacy of the system. Nonetheless, achieving the measured signal amplitudes with these relatively low powers during the concept phase is a good sign that this technology has the potential to meet the biomedical requirements for the use of CW lasers.

As explained in the methods and results section, the coating is not accounted for in the theory. Here again the model could be extended to include a more detailed treatment of the water and water/air interface dynamics. It is however more relevant to develop this modification for more common coatings, such as phospholipid, which does not apply for the

present test system. Also, the stabilization of these bubble was assured by the presence of BSA. It is possible that heat induced a denaturation of the BSA while the oscillations would prevent a stiff reticulation. This effect was not investigated and not accounted for since it has a limited interest for this proof of concept. It would, however, become important in a next step where the obtained damping coefficient is explained in details.

The damping of the oscillations sustained by these BSA-stabilized microbubbles is larger than that predicted for a surfactant-free bubble. It is however interesting to note that the presence of a low viscosity oil layer is sufficient, in principle, to significantly decrease viscous damping. This conclusion also applies to the case of ultrasound-driven bubbles, which offers interesting leads for the design of even more efficient acoustic (and photoacoustic) contrast agents.

The CW laser in this study was modulated using a sine wave for practical simplicity. In theory, a square wave is expected to induce a slightly higher response and to also generate different harmonic response peaks. A more simple sine modulation containing a single harmonic frequency seemed therefore more suited for a proof of concept study where unexpected effects have to be pointed out, but this should be explored further in future work.

VI. CONCLUSIONS

In this study, we have fabricated two types of oil-coated microbubbles, one with dichloromethane and a second type with toluene. In both cases, the oil entraps a dye that absorbs the laser light. The bubbles were first irradiated with a pulsed laser and good agreement between the measured natural frequency and the theoretical predictions was found. The non-dimensional damping coefficient was also measured and shown to be higher than that expected for an oil-coated microbubble. There was also considerable variation from one bubble to another. The microbubbles could successfully be driven by a modulated CW laser irradiation and displayed the expected resonance behavior associated with strong and non-linear acoustic emissions. The microbubble response was seen to vary with repeated laser pulses, with up to a 60% change in response amplitude being recorded for individual microbubbles, which is attributed to a modification of the dye/oil structure within the coating of the bubble. Under CW laser irradiation individual microbubbles also displayed considerable variation in behavior, mostly in their resonant size, with some bubbles growing from

sub-resonant to super-resonant size during exposure. Despite this variability, there was still good agreement with the theoretical predictions for the overall behavior of the microbubble population. The microbubbles exhibited stronger nonlinear behavior than expected, manifested in the generation of acoustic emissions at harmonic and subharmonic frequencies. In particular a sub-population of bubbles $\sim 10\%$ larger than the resonant size generated significant subharmonics, possibly due to period doubling behavior. These surprising results may be of significant interest for contrast-enhanced photoacoustic imaging.

ACKNOWLEDGMENTS

This project was made possible by the funding of NanoNextNL, a micro and nanotechnology consortium of the Government of the Netherlands and 130 partners project and the UK Engineering and Physical Sciences Research Council (grant EP/I021795/1). We also warmly thank Gert-Wim Bruggert, Martin Bos and Bas Benschop for their ongoing and effective technical support.

-
- [1] E. M. Stroh, E. S. L. Berndl, and M. C. Kolios, “High frequency label-free photoacoustic microscopy of single cells,” *Photoacoustics* **1**, 49–53 (2013).
- [2] S. Manohar, S. E. Vaartjes, J. C. G. van Hespén, J. M. Klaase, F. M. van den Engh, W. Steenbergen, and T. G. van Leeuwen, “Initial results of in vivo non-invasive cancer imaging in the human breast using near-infrared photoacoustics,” *Optics Express* **15**, 12277–12285 (2007).
- [3] A. G. Bell, “Upon the production and reproduction of sound by light,” *American Journal of Science* **118**, 404–426 (1980).
- [4] M. Nasiriavanaki and J. Xia and H. Wan and A. Q. Bauer and J. P. Culver and L. V. Wang, “High-resolution photoacoustic tomography of resting-state functional connectivity in the mouse brain,” *PNAS* **111**, 21–26 (2014).
- [5] H.F. Zhang and K. Maslov and G. Stoica and L.V. Wang, “Functional photoacoustic microscopy for high-resolution and noninvasive in vivo imaging,” *Nat. Biotechnol.* **24**, 848–851 (2006).
- [6] W. Lu, Q. Huang, G. Ku, X. Wen, M. Zhou, D. Guzatov, P. Brecht, R. Su, A. Oraevsky, L. V. Wang, and C. Li, “Photoacoustic imaging of living mouse brain vasculature using hollow gold nanospheres,” *Biomaterials* **31**, 2617–2626 (2010).
- [7] A. P. Jathoul, J. Laufer, O. Ogunlade, B. Treeby, B. Cox, E. Zhang, P. Johnson, A. R. Pizzey, B. Philip, T. Marafioti, M. F. Lythgoe, R. B. Pedley, M. A. Pule, and P. Beard, “Deep in vivo photoacoustic imaging of mammalian tissues using a tyrosinase-based genetic reporter,” *Nat. Photon.* **9**, 239–246 (2015).
- [8] B. Nikoobakht and M. A. El-Sayed, “Preparation and Growth Mechanism of Gold Nanorods (NRs) Using Seed-Mediated Growth Method,” *Chem. Mater* **15**, 1957–1962 (2003).
- [9] P. K. Jain and K. S. Lee and I. H. El-Sayed and M. A. El-Sayed, “Calculated Absorption and Scattering Properties of Gold Nanoparticles of Different Size, Shape, and Composition: Applications in Biological Imaging and Biomedicine,” *J. Phys. Chem. B* **110**, 7238–7248 (2006).
- [10] S. Kaul, “Myocardial Contrast Echocardiography A 25-Year Retrospective,” *New Drugs and Technologies* , 291–308 (2015).
- [11] S. Qin and C. F. Caskey and K. W. Ferrara, “Ultrasound contrast microbubbles in imaging and therapy: physical principles and engineering,” *Phys. Med. Biol.* **54** (2009).

- [12] G. Lajoinie, E. Gelderblom, C. Chlon, M. Böhmer, W. Steenbergen, N. de Jong, S. Manohar, and M. Versluis, “Ultrafast vapourization dynamics of laser-activated polymeric microcapsules,” *Nat Commun* **5** (2014).
- [13] K. Wilson, K. Homan, and S. Emelianov, “Biomedical photoacoustics beyond thermal expansion using triggered nanodroplet vaporization for contrast-enhanced imaging,” *Nat. Commun.* **3**, doi: 10.1038/ncomms1627 (2012).
- [14] M. Schwarz, A. Buehler, J. Aguirre, and V. Ntziachristos, “Three-dimensional multispectral optoacoustic mesoscopy reveals melanin and blood oxygenation in human skin in vivo”, *Journal of Biophotonics* **9**, 55–60 (2016).
- [15] J. Zeng, M. Cheng, Y. Wang, L. Wen, L. Chen, Z. Li, Y. Wu, M. Gao, and Z. Chai, “ph-responsive fe(iii)gallic acid nanoparticles for in vivo photoacoustic-imaging-guided photothermal therapy”, *Advanced Healthcare Materials* **5**, 772–780 (2016).
- [16] C. Sun, L. Wen, J. Zeng, Y. Wang, Q. Sun, L. Deng, C. Zhao, and Z. Li, “One-pot solventless preparation of PEGylated black phosphorus nanoparticles for photoacoustic imaging and photothermal therapy of cancer”, *Biomaterials* **91**, 81 – 89 (2016).
- [17] J. D. Dove, T. W. Murray, and M. A. Borden, “Enhanced photoacoustic response with plasmonic nanoparticle-templated microbubbles,” *Soft Matter* **9**, 7743–7750 (2013).
- [18] J. D. Dove, M. A. Borden, and T. W. Murray, “Optically induced resonance of nanoparticle-loaded microbubbles,” *Opt. Lett.* **39**, 3732–3735 (2014).
- [19] J. D. Dove, P. A. Mountford, T. W. Murray, and M. A. Borden, “Engineering optically triggered droplets for photoacoustic imaging and therapy,” *Biomed. Opt. Express* **5**, 4417–4427 (2014).
- [20] M. J. Benchimol, M. J. Hsu, C. E. Schutt, D. J. Hall, R. F. Mattrey, and S. C. Esener, “Phospholipid/carbocyanine dye-shelled microbubbles as ultrasound-modulated fluorescent contrast agents,” *Soft Matter* **9**, 2384–2388 (2013).
- [21] G. Lalwani, X. Cai, L. Nie, L. V. Wang, and B. Sitharaman, “Graphene-based contrast agents for photoacoustic and thermoacoustic tomography”, *Photoacoustics* **1**, 62 – 67 (2013).
- [22] L. M. Tay and C. Xu, “Coating microbubbles with nanoparticles for medical imaging and drug delivery”, *Nanomedicine* **12**, 91–94 (2016).
- [23] A. J. Dixon, S. Hu, A. L. Klibanov, and J. A. Hossack, “Oscillatory dynamics and in vivo photoacoustic imaging performance of plasmonic nanoparticle-coated microbubbles”, *Small*

(Weinheim an der Bergstrasse, Germany) **11**, 3066–3077 (2015).

- [24] H. Moon, J. Kang, C. Sim, J. Kim, H. Lee, J. H. Chang, and H. Kim, “Multifunctional theranostic contrast agent for photoacoustics- and ultrasound-based tumor diagnosis and ultrasound-stimulated local tumor therapy”, *Journal of Controlled Release* **218**, 63–71 (2015).
- [25] Y. Tournia, F. Domenici, S. Orlanducci, F. Mura, D. Grishenkov, P. Trochet, S. Lacerenza, F. Bordini, and G. Paradossi, “Graphene meets microbubbles: A superior contrast agent for photoacoustic imaging”, *ACS Appl. Mater. Interfaces* **8**, 16465–16475 (2016).
- [26] W. Wang and A. Mandelis, “Snr and contrast enhancement techniques for the photoacoustic radar imaging”, *International Journal of Thermophysics* **37**, 74 (2016).
- [27] G. Langer, B. Buchegger, J. Jacak, T. A. Klar, and T. Berer, “Frequency domain photoacoustic and fluorescence microscopy”, *Biomedical Optics Express* **7**, 2692–2702 (2016).
- [28] R. Alwi, S. Telenkov, A. Mandelis, T. Leshuk, F. Gu, S. Oladepo, and K. Michaelian, “Silica-coated super paramagnetic iron oxide nanoparticles (spion) as biocompatible contrast agent in biomedical photoacoustics”, *Biomedical Optics Express* **3**, 2500–2509 (2012).
- [29] Y. Danan, N. ozana, and Z. Zalevsky, “Self periodically heated-cooled nanostructure for photoacoustic imaging with cw illumination”, in *Imaging and Applied Optics 2016*, IW5F.2 (Optical Society of America, Heidelberg) (2016).
- [30] Y. Tanaka, C. Purtil, T. Tajima, M. Seyama, and H. Koizumi, “Sensitivity improvement on cw dual-wavelength photoacoustic spectroscopy using acoustic resonant mode for noninvasive glucose monitor”, in *2016 IEEE SENSORS*, 1–3 (Oct. 30 2016–Nov. 3 2016).
- [31] Kenneth Kroenlein, Chris D. Muzny, Andrei F. Kazakov, Vladimir Diky, Robert D. Chirico, Joseph W. Magee, Ilmutdin Abdulagatov, and Michael Frenkel, “NIST Chemistry WebBook, NIST Standard Reference ,” available at <http://wtt-pro.nist.gov> , (last checked: 16 March 2017).
- [32] Heike Kahl, Tino Wadewitz, and Jochen Winkelmann “Surface Tension of Pure Liquids and Binary Liquid Mixtures,” *J. Chem. Eng. Data* **48**, 580-586 (2003).
- [33] Laurier L Schramm, and Loren G. Hepler “Surface and interfacial tensions of aqueous dispersions of charged colloidal (clay) particles,” *Can. J. Chem* **72**, 1915-1920 (1994).
- [34] M. Alpbaz, A. Tutkun, and O. Bilgesu “The measurement of interfacial tension by drop-weight method,” *Commun. Fac. Sci. Univ. Ank. Serie B* **34**, 103-112 (1988).

- [35] “The Engineering Toolbox,” available at <http://www.engineeringtoolbox.com/>, (last checked: 16 March 2017).
- [36] C. T. Chin, C. Lancée, J. Borsboom, F. Mastik, M. E. Frijlink, N. de Jong, M. Versluis, and D. Lohse, “Brandaris 128: A digital 25 million frames per second camera with 128 highly sensitive frames,” *Rev. Sci. Instr.* **74**, 5026–5034 (2003).
- [37] E. C. Gelderblom, H. J. Vos, F. Mastik, T. Faez, Y. Luan, T. J. A. Kokhuis, A. F. W. van der Steen, D. Lohse, N. de Jong, and M. Versluis, “Brandaris 128 ultra-high-speed imaging facility: 10 years of operation, updates, and enhanced features,” *Rev. Sci. Instr.* **83**, 103706 (2012).
- [38] John J. D’Azzo, Constantine H. Houpis, and Stuart N. Sheldon, “Linear Control System Analysis and Design, Fifth Edition, Revised and Expanded,” CRC Press **ch. 4**, ISBN: 978-0-8247-4038-2 (2003).
- [39] Jason L. Raymond, Ying Luan, Tom van Rooij, Klazina Kooiman, Shao-Ling Huang, David D. McPherson, Michel Versluis, Nico de Jong, and Christy K. Holland, “Impulse response method for characterization of echogenic liposomes,” *J. Acoust. Soc. Am.* **137**, 16931703 (2015).
- [40] X. Chen, K. Q. Schwarz, and K. J. Parker, “Acoustic coupling from a focused transducer to a flat plate and back to the transducer,” *J. Acoust. Soc. Am.* **95**, 3049–3054 (1994).
- [41] See supplementary material at [URL will be inserted by AIP] for response of a 3.0 micrometer toluene-coated bubble irradiated by a pulsed laser. Movie recorded at 10 million frames per second.
- [42] See supplementary material at [URL will be inserted by AIP] for response of a 3.4 micrometer DCM-coated bubble irradiated by a pulsed laser. Movie recorded at 10 million frames per second.
- [43] See supplementary material at [URL will be inserted by AIP] for the response of a 2.2 micrometer DCM-coated bubble irradiated by a CW laser modulated at 1.0 MHz. Movie recorded at 10 million frames per second.
- [44] See supplementary material at [URL will be inserted by AIP] for the response of a 4.2 micrometer toluene-coated bubble irradiated by a CW laser modulated at 0.75 MHz. Movie recorded at 10 million frames per second.

- 530 [45] J. Sijl, B. Dollet, M. Overvelde, V. Garbin, T. Rozendal, N. de Jong, D. Lohse, and M. Versluis,
531 “Subharmonic behavior of phospholipid-coated ultrasound contrast agent microbubbles,” J.
532 Acoust. Soc. Am. **128**, 3239–3252 (2010).
- 533 [46] I. Standard IEC, “Safety of laser products—Part 1: Equipment classification, requirements
534 and user’s guide, IEC Geneva, Switzerland,” (2001).

1. Momentum equation

The Navier-Stokes equation for an incompressible, Newtonian fluid is as follows

$$\rho \frac{Dv}{Dt} = -\nabla P + \rho g + \mu \nabla^2 v$$

Body forces will be negligible and a spherical symmetry case is investigated leading to

$$\rho \left(\frac{\partial v}{\partial t} + v \frac{\partial v}{\partial r} \right) = -\frac{\partial P}{\partial r} + \mu \nabla^2 v$$

In the simulation, the bubbles will have an oscillation amplitude in the order of micrometers and the frequency will be in the order of MHz. Speeds will therefore be approximately $1m.s^{-1}$ and thus much lower than the speed of sound. For this reason, incompressibility of the liquid is assumed leading to:

$$v = \frac{\dot{R}R^2}{r^2} \vec{e}_r$$

Where \dot{R} is $\frac{dR}{dt}$. With this we find

$$\begin{aligned} \rho \left(\frac{1}{r^2} \frac{\partial}{\partial t} (\dot{R}R^2) - 2 \frac{(\dot{R}R^2)^2}{r^5} \right) &= -\frac{\partial P}{\partial r} + \mu \nabla^2 v \\ -\frac{1}{\rho(r)} \left(\frac{\partial P}{\partial r} + \mu \nabla^2 v \right) &= \frac{1}{r^2} \frac{d}{dt} (\dot{R}R^2) - \frac{2(\dot{R}R^2)^2}{r^5} \end{aligned}$$

This equation can be written for both the oil layer and the water. When integrating from $r = A$ to $r = B$ the term $\mu \nabla^2 v$ drops out and this gives

$$\frac{P(B) - P(A)}{\rho} = \left[\frac{1}{r} \frac{d}{dt} (\dot{R}R^2) - \frac{1}{2} \frac{(\dot{R}R^2)^2}{r^4} \right]_A^B$$

$$\frac{P(B) - P(A)}{\rho} = \left[\frac{\ddot{R}R^2}{r} + \frac{2\dot{R}^2 R}{r} - \frac{1}{2} \frac{\dot{R}^2 R^4}{r^4} \right]_A^B$$

537 Taking the inner bubble radius R_i for R and integrating over the water domain:

$$P(R_e^+) - P_\infty = \rho_w \left(\frac{\ddot{R}_i R_i^2 + 2\dot{R}_i^2 R_i}{R_e} - \frac{1}{2} \frac{\dot{R}_i^2 R_i^4}{R_e^4} \right) \quad (\text{A1})$$

538 Integrating over the oil domain:

$$P(R_e^-) - P(R_i^+) = \rho_o \left(\frac{\ddot{R}_i R_i^2 + 2\dot{R}_i^2 R_i}{R_e} - \frac{1}{2} \frac{\dot{R}_i^2 R_i^4}{R_e^4} - \left(\frac{\ddot{R}_i R_i^2 + 2\dot{R}_i^2 R_i}{R_i} - \frac{1}{2} \frac{\dot{R}_i^2 R_i^4}{R_i^4} \right) \right) \quad (\text{A2})$$

539 rewritten as:

$$P(R_i^+) - P(R_e^-) = \rho_o \left((\ddot{R}_i R_i^2 + 2\dot{R}_i^2 R_i) \left(\frac{1}{R_i} - \frac{1}{R_e} \right) - \frac{1}{2} \dot{R}_i^2 R_i \left(\frac{1}{R_i^4} - \frac{1}{R_e^4} \right) \right) \quad (\text{A3})$$

540 2. Normal component stress tensor

Over the oil gas interface

$$\overline{\overline{\sigma}}_o \cdot \vec{e}_r - \overline{\overline{\sigma}}_g \cdot \vec{e}_r = \delta P_1$$

541 Where $\overline{\overline{\sigma}}_o$ is the strain tensor and \vec{e}_r denotes that it is in the r direction. δP_1 is the difference
542 in pressure over the oil-gas interface.

$$2\mu_o u'(R_i) - P(R_i^+) + P_g = \frac{2\sigma_o}{R_i}$$

543 Where u' is the velocity derivative to the radius. σ is the surface tension. Knowing $v =$
544 $\dot{R}_i R_i^2 / r^2$ we also know $v'(R_i) = -2\dot{R}_i R_i^2 / R_i^3$

$$-4\mu_o \frac{\dot{R}_i R_i^2}{R_i^3} - P(R_i^+) + P_g = \frac{2\sigma_o}{R_i}$$

$$P_g - P(R_i^+) = 4\mu_o \frac{\dot{R}_i}{R_i} + \frac{2\sigma_o}{R_i} \quad (\text{A4})$$

Over the oil water interface

$$\overline{\overline{\sigma}}_w \cdot \vec{e}_r - \overline{\overline{\sigma}}_o \cdot \vec{e}_r = \delta P_2$$

$$[2\mu_w v'(R_e) - P(R_e^+)] - [2\mu_o v'(R_e) - P(R_e^-)] = \frac{2\sigma_{wo}}{R_e}$$

Knowing $v = \dot{R}_i R_i^2 / r^2$ we also know $v'(R_e) = -2\dot{R}_i R_i^2 / R_e^3$. Rewriting the equation above then gives

$$\begin{aligned} \left[\frac{-4\dot{R}_i R_i^2}{R_e^3} \mu_w - P(R_e^+) \right] - \left[\frac{-4\dot{R}_i R_i^2}{R_e^3} \mu_o - P(R_e^-) \right] &= \frac{2\sigma_{wo}}{R_e} \\ \frac{-4\dot{R}_i R_i^2}{R_e^3} (\mu_w - \mu_o) - \frac{2\sigma_{wo}}{R_e} &= P(R_e^+) - P(R_e^-) \end{aligned}$$

Resulting in

$$P(R_e^+) - P(R_e^-) = \frac{4\dot{R}_i R_i^2}{R_e^3} (\mu_o - \mu_w) - \frac{2\sigma_{wo}}{R_e} \quad (\text{A5})$$

3. Combining

We know that $P_g - P_\infty = P(R_i^-) - P_\infty$ because the pressure at the inside of the inner radius of the bubble is by definition in the gas and therefore $P_g = P(R_i^-)$. We can rewrite by adding and subtracting similar terms

$$P_g - P_\infty = \underbrace{P_g(R_i^-) - P(R_i^+)} + \underbrace{P(R_i^+) - P(R_e^-)} + \underbrace{P(R_e^-) - P(R_e^+)} + \underbrace{P(R_e^+) - P_0} \quad (\text{A6})$$

Part 1 of (A6) is defined in (A4), part 2 is defined in (A3), part 3 is defined in (A5) and part 4 is defined in (A1). Thus, the complete equation is:

$$\begin{aligned}
P_g - P_\infty = 4\mu_o \frac{\dot{R}_i}{R_i} + \frac{2\sigma_o}{R_i} + \rho_o \left((\ddot{R}_i R_i^2 + 2\dot{R}_i^2 R_i) \left(\frac{1}{R_i} - \frac{1}{R_e} \right) \right. \\
\left. - \frac{1}{2} \dot{R}_i^2 R_i^4 \left(\frac{1}{R_i^4} - \frac{1}{R_e^4} \right) \right) - \frac{4\dot{R}_i R_i^2}{R_e^3} (\mu_o - \mu_w) \\
+ \frac{2\sigma_{wo}}{R_e} + \rho_w \left(\frac{\ddot{R}_i R_i^2 + 2\dot{R}_i^2 R_i}{R_e} - \frac{1}{2} \frac{\dot{R}_i^2 R_i^4}{R_e^4} \right) \quad (A7)
\end{aligned}$$

Rewriting gives

$$\begin{aligned}
P_g - P_\infty = \ddot{R}_i \left[\rho_o R_i^2 \left(\frac{1}{R_i} - \frac{1}{R_e} \right) + \rho_w \frac{R_i^2}{R_e} \right] \\
+ \rho_o \left[2R_i^2 R_i \left(\frac{1}{R_i} - \frac{1}{R_e} \right) - \frac{1}{2} \dot{R}_i^2 R_i^4 \left(\frac{1}{R_i^4} - \frac{1}{R_e^4} \right) \right] \\
+ \rho_w \left[2 \frac{\dot{R}_i^2 R_i}{R_e} - \frac{1}{2} \frac{R_i^2 \dot{R}_i^4}{R_e^4} \right] + 4\mu_o \left[\frac{\dot{R}_i}{R_i} - \frac{\dot{R}_i R_i^2}{R_e^3} \right] + 4 \frac{\dot{R}_i R_i^2}{R_e^3} \mu_w + \frac{2\sigma_{ow}}{R_e} + \frac{2\sigma_o}{R_i} \quad (A8)
\end{aligned}$$

And rewriting further

$$\begin{aligned}
P_g - P_\infty = \ddot{R}_i \left[\frac{R_i^2}{R_e} (\rho_w - \rho_o) + \rho_o R_i \right] \\
+ \rho_o \left[\dot{R}_i^2 R_i \left(\frac{2}{R_i} - \frac{2}{R_e} - \frac{1}{2} \frac{1}{R_i} + \frac{1}{2} \frac{R_i^3}{R_e^4} \right) \right] + \rho_w \left[\frac{\dot{R}_i^2 R_i}{R_e} \left(2 - \frac{1}{2} \frac{R_i^3}{R_e^3} \right) \right] \\
+ 4\mu_o \left[\frac{\dot{R}_i}{R_i} - \frac{\dot{R}_i R_i^2}{R_e^3} \right] + 4 \frac{\dot{R}_i R_i^2}{R_e^3} \mu_w + \frac{2\sigma_{ow}}{R_e} + \frac{2\sigma_o}{R_i} \quad (A9)
\end{aligned}$$

To reach the modified Rayleigh-Plesset equation:

$$\begin{aligned}
P_g - P_\infty = \ddot{R}_i \left[\frac{R_i^2}{R_e} (\rho_w - \rho_o) + \rho_o R_i \right] \\
+ \dot{R}_i^2 R_i \left[\rho_o \left(\frac{3}{2R_i} - \frac{2}{R_e} + \frac{1}{2} \frac{R_i^3}{R_e^4} \right) + \frac{\rho_w}{R_e} \left(2 - \frac{1}{2} \frac{R_i^3}{R_e^3} \right) \right] \\
+ 4\mu_o \left[\frac{\dot{R}_i}{R_i} - \frac{\dot{R}_i R_i^2}{R_e^3} \right] + 4 \frac{\dot{R}_i R_i^2}{R_e^3} \mu_w + \frac{2\sigma_{ow}}{R_e} + \frac{2\sigma_o}{R_i} \quad (A10)
\end{aligned}$$

Where the viscosity of water μ_w is temperature dependent following the following relation

$$\mu_w = 2.414 \cdot 10^{-5} \cdot 10^{247.8/(T-140)}$$

Where T is the temperature of the water at the water-oil interface. This new RP equation comes down to the classic RP equation for a bubble with only one liquid around it when the properties of water and oil are chosen identical.

4. Small variations around equilibrium

In this part small variations are added to the static solution in order to obtain a simple model describing the simulation result. The static solution assumes the temperature in the gas to be homogeneous. For this to be true for a modulated laser signal, the diffusion time of the heat in the gas should be smaller than the half period of the laser modulation. This can be contained in the following equations

$$t = \frac{R_i^2}{\pi D_g} = \frac{\text{Period laser}}{2} = \frac{1}{2f},$$

we make the assumption a priori (verified a posteriori) that the microbubble resonance frequency is in the same range as its acoustic resonance frequency and using a Minnaert approximation, the temperature in the gas can be considered constant for bubbles smaller than:

$$R = \frac{\pi D_g}{6.6} \approx 11 \mu m$$

A diffusion distance estimation can be done for the water to find app. $0.1 \mu m$ for $1 MHz$ frequency.

The change in temperature over time can be described as follows:

$$(\rho_o V_{oil} C_{po} + \rho_w V_{w0.1} C_{pw}) dT = B_a(t) V_{oil} dt,$$

with ρ_o the density of the oil, $V_{w0.1}$ the volume of the first $0.1 \mu m$ of water, c_{po} the heat capacity at constant pressure of the oil, B_0 the maximum power of the laser and B the absorbed laser power ($W.m^{-3}$).

$$\frac{dT}{dt} = \frac{B_a(t)V_{oil}}{\rho_o V_{oil}C_{po} + \rho_w V_{w0.1}C_{pw}} \quad (A11)$$

$$\rightarrow T_g = \frac{\int_0^t B_a(t)dtV_{oil}}{(\rho_o V_{oil}C_{po} + \rho_w V_{w0.1}C_{pw})} + \text{constant} \quad (A12)$$

with B_{amp} being the amplitude of the oscillations in the power and $\omega = 2\pi f$. Using the initial equilibrium solution:

$$T_g = \frac{\int_0^t B_a(t)dtV_{oil}}{(\rho_o V_{oil}C_{po} + \rho_w V_{w0.1}C_{pw})} + \frac{-B_{a,av}R_{i,eq}^2}{6\lambda_o} - \frac{C_{1o}}{R_{i,eq}} + C_{2o} + T_{room}$$

570 I is the average laser power. Filling in C_{1o} and C_{2o} and rewriting gives

$$\begin{aligned} T_g = & \frac{\int_0^t B_a(t)dtV_{oil}}{(\rho_o V_{oil}C_{po} + \rho_w V_{w0.1}C_{pw})} \\ & + \frac{-B_{a,av}R_{i,eq}^2}{6\lambda_o} - \frac{B_{a,av}R_{i,eq}^2}{3\lambda_o} + \frac{B_{a,av}R_{i,eq}^3}{3\lambda_o R_{e,eq}} \left(1 - \frac{\lambda_o}{\lambda_w}\right) + \frac{B_{a,av}R_{e,eq}^2}{3\lambda_o} \left(0.5 + \frac{\lambda_o}{\lambda_w}\right) + T_{room} \end{aligned} \quad (A13)$$

$$\begin{aligned} \rightarrow T_g = & \frac{\int_0^t B_a(t)dtV_{oil}}{(\rho_o V_{oil}C_{po} + \rho_w V_{w0.1}C_{pw})} + \\ & \frac{B_{a,av}}{3\lambda_o} \left(-1.5R_{i,eq}^2 + \frac{R_{i,eq}^3}{R_{e,eq}} \left(1 - \frac{\lambda_o}{\lambda_w}\right) + R_{e,eq}^2 \left(0.5 + \frac{\lambda_o}{\lambda_w}\right) \right) + T_{room} \end{aligned} \quad (A14)$$

571 We know that

$$P = \frac{P_0 V_0 T_g}{T_0 \frac{4}{3} \pi R_i^3} \quad (A15)$$

Where T_g can be filled in and P is the total pressure as used in the modified Rayleigh-Plesset equation (eq A10) :

$$\begin{aligned} P_g - P_\infty = & \ddot{R}_i \left[\frac{R_i^2}{R_e} (\rho_w - \rho_o) + \rho_o R_i \right] + \dot{R}_i^2 R_i \left[\rho_o \left(\frac{3}{2R_i} - \frac{2}{R_e} + \frac{1}{2} \frac{R_i^3}{R_e^4} \right) \right. \\ & \left. + \frac{\rho_w}{R_e} \left(2 - \frac{1}{2} \frac{R_i^3}{R_e^3} \right) \right] + 4\mu_o \left[\frac{\dot{R}_i}{R_i} - \frac{\dot{R}_i R_i^2}{R_e^3} \right] + 4 \frac{\dot{R}_i R_i^2}{R_e^3} \mu_w + \frac{2\sigma_{ow}}{R_e} + \frac{2\sigma_o}{R_i} \end{aligned} \quad (A16)$$

Where P_g is the found P and P_∞ is the pressure at infinity. Expressing this in the new variables P_0 as the pressure at the beginning of the static solution and P_g as the total pressure in the gas, and filling in T_g and the found pressure, this gives:

$$\begin{aligned} \frac{P_0 R_{i,0}^3}{T_0 R_i^3} & \left[\frac{\int_0^t B_a(t) dt V_{oil}}{\rho_o V_{oil} c p_o + \rho_w V_{w0.1} c p_w} \right. \\ & + \frac{B_{a,av}}{3\lambda_o} \left(-1.5 R_{i,eq}^2 + \frac{R_{i,eq}^3}{R_{e,eq}} \left(1 - \frac{\lambda_o}{\lambda_w} \right) + R_{e,eq}^2 \left(0.5 + \frac{\lambda_o}{\lambda_w} \right) \right) + T_{room} \Big] \\ & - P_\infty = \ddot{R}_i \left[\frac{R_i^2}{R_e} (\rho_w - \rho_o) + \rho_o R_i \right] + \dot{R}_i^2 R_i \left[\rho_o \left(\frac{3}{2R_i} - \frac{2}{R_e} + \frac{1}{2} \frac{R_i^3}{R_e^4} \right) \right. \\ & \left. + \frac{\rho_w}{R_e} \left(2 - \frac{1}{2} \frac{R_i^3}{R_e^3} \right) \right] + 4\mu_o \left[\frac{\dot{R}_i}{R_i} - \frac{\dot{R}_i R_i^2}{R_e^3} \right] + 4 \frac{\dot{R}_i R_i^2}{R_e^3} \mu_w + \frac{2\sigma_{ow}}{R_e} + \frac{2\sigma_o}{R_i} \quad (A17) \end{aligned}$$

Organizing for \dot{R} , \dot{R}^2 and \ddot{R} and, as an approximation, taking all R_i and R_e to be $R_{i,eq}$ and $R_{e,eq}$ in case they are multiplied by \dot{R} , \dot{R}^2 or \ddot{R} .

$$\begin{aligned} \int B dt & \underbrace{\left[\frac{P_0 V_0}{T_0 \frac{4}{3} \pi R_{i,eq}^3 \left(\rho_o C_{p_o} + \rho_w \frac{V_{w0.1}}{V_{oil}} C_{p_w} \right)} \right]}_{\alpha} + \frac{P_0 V_0}{T_0 \frac{4}{3} \pi R_i^3} [T_{gas,eq} + T_{room}] - P_\infty \\ & = \ddot{R}_i \underbrace{\left[\frac{R_{i,eq}^2}{R_{e,eq}} (\rho_w - \rho_o) + \rho_o R_{i,eq} \right]}_{\beta} \\ & + \underbrace{\dot{R}_i^2 R_{i,eq} \left[\rho_o \left(\frac{3}{2R_{i,eq}} - \frac{2}{R_{e,eq}} + \frac{1}{2} \frac{R_{i,eq}^3}{R_{e,eq}^4} \right) + \frac{\rho_w}{R_{e,eq}} \left(2 - \frac{1}{2} \frac{R_{i,eq}^3}{R_{e,eq}^3} \right) \right]}_{\gamma} \\ & + \underbrace{\dot{R}_i \left[4 \left(\frac{\mu_o}{R_{i,eq}} + \frac{R_{i,eq}^2}{R_{e,eq}^3} (\mu_w - \mu_o) \right) \right]}_{\delta} + 2 \frac{\sigma_{ow}}{R_e} + \frac{\sigma_o}{R_i} \quad (A18) \end{aligned}$$

In order to find an equation that does not contain an integral, everything is derived to time.

$$\alpha B - \underbrace{3 \frac{P_0 T_{g2}}{T_0} \frac{R_{i,0}}{R_{i,eq}^4}}_{\zeta} \dot{R}_i = \ddot{R}_i \beta + 2\gamma \ddot{R}_i \dot{R}_i + \delta \ddot{R}_i + 2\dot{R}_i \underbrace{\left(\frac{-\sigma_{ow}}{R_e^2} + \frac{-\sigma_o}{R_i^2} \right)}_{\epsilon} \quad (\text{A19})$$

$$\alpha B - \zeta \dot{R}_i = \ddot{R}_i \beta + 2\gamma \ddot{R}_i \dot{R}_i + \delta \ddot{R}_i + 2\dot{R}_i \epsilon \quad (\text{A20})$$

579 In which case \dot{R}_e is assumed to be approximately \dot{R}_i and $T_{gas,eq} + T_{room}$ is now called T_{g2} .
 580 The term $2\gamma \ddot{R}_i \dot{R}_i$ is of higher order and is therefore neglected. R_i is expected to act as an
 581 harmonic oscillator and will therefore have the shape of

$$R_i = R_{i,eq} + r_i e^{j\omega t} + \varphi = R_{i,eq} + \underline{r\dot{i}} \quad (\text{A21})$$

$$\dot{R}_i = j\omega r_i e^{j\omega t} + \varphi = (j\omega) \underline{r\dot{i}} \quad (\text{A22})$$

$$\ddot{R}_i = -\omega^2 r_i e^{j\omega t} + \varphi = (j\omega)^2 \underline{r\dot{i}} \quad (\text{A23})$$

$$\ddot{\ddot{R}}_i = -j\omega^3 r_i e^{j\omega t} + \varphi = (j\omega)^3 \underline{r\dot{i}} \quad (\text{A24})$$

$$\alpha B = j\omega r_i [2\epsilon + \zeta + j\omega\delta - \omega^2\beta] \quad (\text{A25})$$

$$\frac{r_i}{B} = \frac{\alpha/(2\epsilon + \zeta)}{j\omega \left[1 + j\omega \frac{\delta}{2\epsilon + \zeta} - \omega^2 \frac{\beta}{2\epsilon + \zeta} \right]} \quad (\text{A26})$$

587 Which has the shape of a transfer function

$$\frac{O}{I} = \frac{G}{1 + j\omega \frac{2z}{\omega_0} - \frac{\omega^2}{\omega_0^2}} \cdot \frac{1}{j\omega} \quad (\text{A27})$$

588 with G being the gain, O the output, I the input, z the damping and ω_0 the angular eigen
 589 frequency. One thing that can be noted here is that this transfer function is of third order
 590 where a standard RP equation would be of second order. The expected phase difference in

our case is therefore π at resonance instead of $\pi/2$ such as in the normal RP equation.

$$\rightarrow \omega_0 = \sqrt{\frac{2\epsilon + \zeta}{\beta}} = \sqrt{\frac{-2 \left(\frac{\sigma_{ow}}{R_e^2} + \frac{\sigma_o}{R_i^2} \right) + 3 \frac{P_0 T_{g2}}{T_0} \frac{R_{i,0}}{R_{i,eq}^4}}{\frac{R_{i,eq}^2}{R_{e,eq}} (\rho_w - \rho_o) + \rho_o R_{i,eq}}} \quad (\text{A28})$$

From (A15) we can find

$$\frac{T_{g2} R_{i,0}^3}{R_{i,eq}^4} = \frac{T_0 P_{g,eq}}{P_0 R_{i,eq}} \quad (\text{A29})$$

Therefore ζ can be simplified

$$\zeta = 3 \frac{P_0 T_{g2} R_{i,0}}{T_0 R_{i,eq}^4} = 3 \frac{P_{g,eq}}{R_{i,eq}} \quad (\text{A30})$$

Where the equilibrium pressure $P_{g,eq}$ is the atmospheric pressure plus the Laplace pressure jump over both interfaces:

$$\zeta = 3 \left(\frac{P_{atm}}{R_{i,eq}} + \frac{2\sigma_o}{R_{i,eq}^2} + \frac{2\sigma_{ow}}{R_{i,eq} R_{e,eq}} \right) \quad (\text{A31})$$

$$\rightarrow \omega_0 = \sqrt{\frac{-2 \left(\frac{\sigma_{ow}}{R_{e,eq}^2} + \frac{\sigma_o}{R_{i,eq}^2} \right) + 3 \left(\frac{P_{atm}}{R_{i,eq}} + \frac{2\sigma_o}{R_{i,eq}^2} + \frac{2\sigma_{ow}}{R_{i,eq} R_{e,eq}} \right)}{\frac{R_{i,eq}^2}{R_{e,eq}} (\rho_w - \rho_o) + \rho_o R_{i,eq}}} \quad (\text{A32})$$

ω_0 is not a function of time so all R_i and R_e are now $R_{i,eq}$ and $R_{e,eq}$.

$$\rightarrow \omega_0 = \sqrt{\frac{\frac{4\sigma_o}{R_{i,eq}^2} + 2\sigma_{ow} \left(\frac{-1}{R_{e,eq}^2} + \frac{3}{R_{i,eq} R_{e,eq}} \right) + \frac{3P_{atm}}{R_{i,eq}}}{\frac{R_{i,eq}^2}{R_{e,eq}} (\rho_w - \rho_o) + \rho_o R_{i,eq}}} \quad (\text{A33})$$

$$\rightarrow \omega_0 = \sqrt{\frac{\frac{1}{R_{i,eq}} \left(\frac{4\sigma_o}{R_{i,eq}} + 2\sigma_{ow} \left(\frac{-R_{i,eq}}{R_{e,eq}^2} + \frac{3}{R_{e,eq}} \right) + 3P_{atm} \right)}{R_{i,eq} \left(\frac{R_{i,eq}}{R_{e,eq}} (\rho_w - \rho_o) + \rho_o \right)}} \quad (\text{A34})$$

$$\rightarrow \omega_0 = \frac{1}{R_{i,eq}} \sqrt{\frac{\frac{4\sigma_o}{R_{i,eq}} + 2\sigma_{ow} \left(\frac{-R_{i,eq}}{R_{e,eq}^2} + \frac{3}{R_{e,eq}} \right) + 3P_{atm}}{\frac{R_{i,eq}}{R_{e,eq}}(\rho_w - \rho_o) + \rho_o}} \quad (\text{A35})$$

which altogether is an expression for the angular eigenfrequency as a function of $R_{i,eq}$ and $R_{e,eq}$. This shows the eigenfrequency is inversely related to the bubble size but also shows that the oil layer thickness plays a role. The denominator under the square root shows an inertial shift of the resonance curve: Because oil and water have different densities, the thickness of the oil layer influences the mass to be displaced and therefore the resonance frequency.

Now to find an expression for the damping. According to A27:

$$\frac{2z}{\omega_0} = \frac{\delta}{2\epsilon + \zeta} \quad (\text{A36})$$

607

$$\omega_0 = \sqrt{\frac{2\epsilon + \zeta}{\beta}} \quad (\text{A37})$$

608

$$\rightarrow z = \frac{\omega_0}{2} \frac{\delta}{2\epsilon + \zeta} = \frac{1}{2} \frac{\delta}{\sqrt{\beta(2\epsilon + \zeta)}} \quad (\text{A38})$$

609

$$z = \frac{1}{2} \frac{4 \left(\frac{\mu_o}{R_{i,eq}} + \frac{R_{i,eq}^2}{R_{e,eq}^3} (\mu_w - \mu_o) \right)}{\sqrt{\beta(2\epsilon + \zeta)}} \quad (\text{A39})$$

Fig. 1. Schematic of the microbubble system with the three domains and the corresponding physical parameters.

Fig. 2. **a** Schematics of the experimental setup comprising the ultra high-speed camera Brandaris 128, a pulsed or CW laser coupled through a microscope objective, and a 1 MHz ultrasound receiving transducer to record the acoustic emission from the microbubbles. **b** Example of confocal image of an oil-coated microbubble where the oil is labeled with fluorescent Nile Red.

Fig. 3. **a** and **b** Example of response of a DCM-coated (a) and toluene-coated (b) microbubbles to $\sim 50 \text{ mJ/cm}^2$ pulse laser irradiation. The arrival of the laser pulse is indicated by the vertical green line. **c** Frames of the ultra-high speed recording of the event plotted in a. **d** and **e** Theoretical and experimental resonance frequencies of DCM and toluene-coated microbubbles, respectively. R-P in the legend corresponds to the Rayleigh-Plesset equation for a free, acoustically driven bubble.

Fig. 4. **a** Radius-time curve of a DCM-coated microbubble extracted from an ultra high-speed optical recording. **b** and **c** Still frames of the optical recording used to obtain a. **b** is taken from the first movie, before the laser is turned on and shows the 'cold' bubble. **c** is taken from the first laser irradiation and when the radius of the bubble coincides with the average radius. **d** displays the acoustic emission from a DCM-coated microbubble over the full $300 \mu\text{s}$ of laser irradiation recorded by the 1 MHz focused ultrasound transducer. The position in time and duration of the high-speed recording is depicted by the grey rectangle.

Fig. 5. **a,c** and **e** Sample of resonance curves of single microbubbles obtained from a single acoustical recording when a microbubble, heated up by the average irradiating laser power, grows from below the resonant size to above the resonant size. Each color represent a different bubble. **a,c** and **e** correspond to DCM-coated microbubbles irradiated by a 1 MHz and 0.75 MHz modulated CW laser and toluene-coated microbubbles irradiated by a 0.75 MHz modulated CW laser, respectively. **b,d** and **f** show the phases of the oscillations for each curve of **a,c** and **e**, respectively.

Fig. 6. **a** Predicted resonance behavior of a population of DCM-coated microbubbles to a 1 MHz modulated CW laser (red area) given the experimentally measured damping

coefficients for the considered microbubbles. Experimental data extracted from the ultra high-speed recordings are represented with blue error bars. The data in both cases is normalized using the proposed scaling function. **b** Relative phase of the microbubble oscillations corresponding to the data shown in **a**.

Fig. 7. **a,c** and **e** Harmonic generation obtained from the acoustical recordings when a single microbubble, heated up by the average irradiating laser power, grows from below the resonant size to above the resonant size. **a**, **c** and **e** correspond to DCM-coated microbubbles irradiated by a 1 MHz and 0.75 MHz modulated CW laser and toluene-coated microbubbles irradiated by a 0.75 MHz modulated CW laser, respectively. **b,d** and **f** show the sub-harmonic generation in the same order. The x-axis displays the radius of the microbubble normalized by its resonant radius. The emitted pressure is plotted in the vertical (in dB) with the maximum response at the fundamental frequency as a reference.